particles

IMPACT FACTOR 1.7

CITESCORE 3.2

Article

Giant Halo in ^{66}Ca Within Relativistic Continuum Hartree–Bogoliubov Theory Combined with Lipkin–Nogami Method

Chang Zhou, Peng Guo and Xiaofei Jiang

Special Issue
Selected Papers from the "7th Workshop on the Nuclear Mass Table with DRHBc Theory"

Edited by
Dr. Shuangquan Zhang and Dr. Youngman Kim

MDPI

https://doi.org/10.3390/particles7040069 particles

MDPI

Article

Giant Halo in ^{66}Ca Within Relativistic Continuum Hartree–Bogoliubov Theory Combined with Lipkin–Nogami Method

Chang Zhou, **Peng Guo** and **Xiaofei Jiang** *

State Key Laboratory of Nuclear Physics and Technology, School of Physics, Peking University, Beijing 100871, China; c.zhou@pku.edu.cn (C.Z.); 2301110125@pku.edu.cn (P.G.)
* Correspondence: jiangxiaofei@pku.edu.cn

Abstract: The impact of the Lipkin–Nogami (LN) method on a giant halo is investigated within the relativistic continuum Hartree–Bogoliubov (RCHB) theory. The ground-state properties of Ca isotopes obtained from RCHB and RCHB+LN calculations are presented. The results show that the LN correction does not change the range of Ca isotopes with a giant halo. Taking ^{66}Ca as an example, the neutron density distribution with LN correction is found to be slightly more diffused, which can be illustrated by the enlargement of the root mean square radius and the enhancement of the relative contribution in neutron $3s_{1/2}$ level.

Keywords: relativistic continuum Hartree–Bogoliubov theory; Lipkin–Nogami method; Dirac Woods–Saxon basis; giant halo

1. Introduction

The study of exotic nuclei with extreme N/Z ratios has become one of the frontiers of nuclear physics [1–4]. One of the interesting and impressive phenomena in exotic nuclei is the halo, which was first discovered in ^{11}Li [5] and has been observed in many light nuclei near drip lines [6]. Experimentally, some unusual properties have been found in halo nuclei, for example, their abnormally large radii [5], their narrow momentum distribution in the breakup reaction [7,8], the enhancement of electromagnetic dissociation cross-sections [9], etc.

In halo nuclei, the weakly-bound valence nucleons could be easily scattered to the continuum states due to the pairing correlations [10]. Thus, a theory which gives a proper theoretical description of halo phenomena must properly treat the continuum, the pairing correlations, the large spatial distributions, and the coupling among them. The relativistic continuum Hartree–Bogoliubov (RCHB) theory [11] fulfills all these features self-consistently. It has achieved great success in reproducing and interpreting the halo in ^{11}Li [10]. The RCHB theory also predicted the halo nuclei in Zr isotopes with a large amount of particle numbers in the halo region [12]. This special kind of halo is called the giant halo. Giant halo phenomena have also been predicted in Ca isotopes [13,14] within RCHB theory. In addition to RCHB theory, the relativistic mean field–BCS approach combined with proper treatments of the resonant continuum [15–18], the relativistic [19] and non-relativistic [20–22] Hartree–Fock–Bogoliubov theory, and the RCHB theory with the Green's function method [23,24] also give the predictions of giant halos.

In RCHB theory, the pairing correlations are treated with Bogoliubov transformation. However, Bogoliubov transformation breaks the symmetry of the particle number. Thus, it is necessary to investigate the influence of the particle number symmetry breaking on the halo and giant halo. Variation after particle number projection method is a rigorous way to restore the broken symmetry of the particle number [25,26]. However, such calculations are expected to have a massive computational cost for realistic interactions [26,27]. To

check for updates

Citation: Zhou, C.; Guo, P.; Jiang, X. Giant Halo in ^{66}Ca Within Relativistic Continuum Hartree–Bogoliubov Theory Combined with Lipkin–Nogami Method. *Particles* **2024**, *7*, 1128–1138. https://doi.org/10.3390/particles7040069

Academic Editor: Omar Benhar

Received: 25 October 2024
Revised: 16 December 2024
Accepted: 19 December 2024
Published: 21 December 2024

reduce the time consumption, an approximation to the variation after the particle number projection method by means of the Lipkin–Nogami (LN) method [28–30] has been widely used. Up to now, the LN method has been applied in many nuclear studies, such as nuclear charge distributions [31], abnormal odd–even staggering around ^{132}Sn [32], the properties of low-lying states [33,34], superdeformed bands [27,35,36], the thermodynamic properties of nuclei [37], and two-neutrino double beta decay [38].

In this paper, we combine the RCHB theory with the LN method to investigate the giant halo phenomena in Ca isotopes, especially in ^{66}Ca. By comparing the RCHB and RCHB+LN calculations, the impact of the LN correction on giant halos is discussed.

2. Method

2.1. The Relativistic Continuum Hartree–Bogoliubov Theory

The detailed formalism of RCHB theory can be found in Refs. [11,39,40]. The RCHB theory, assuming the spherical symmetry, solves the relativistic Hartree–Bogoliubov (RHB) equations [41] in the coordinate space in order to deal with the large density distribution. Alternatively, one can use a basis with improved asymptotic behavior at large distances [42], for example, the spherical Dirac Woods–Saxon (DWS) basis used here. As shown in Ref. [42], an expansion in the DWS basis is fully equivalent to the calculations in coordinate space. In fact, the DWS basis has already been used in the deformed relativistic Hartree–Bogoliubov theory in continuum (DRHBc) [43], which has many applications so far [44–48]. Our examination shows that the results of RCHB solved in the DWS basis are the same as those of DRHBc with a spherical shape.

The RHB equations self-consistently treat the mean field and pairing correlations,

$$\begin{pmatrix} h_D - \lambda & \Delta \\ -\Delta^* & -h_D^* + \lambda \end{pmatrix} \begin{pmatrix} U_k \\ V_k \end{pmatrix} = E_k \begin{pmatrix} U_k \\ V_k \end{pmatrix}, \tag{1}$$

where λ is the Fermi surface, E_k is the quasiparticle energy, and $(U_k, V_k)^T$ are the quasiparticle wave functions. The Dirac Hamiltonian h_D in coordinate space reads as

$$h_D(\boldsymbol{r}) = \boldsymbol{\alpha} \cdot \boldsymbol{p} + V(\boldsymbol{r}) + \beta[M + S(\boldsymbol{r})], \tag{2}$$

with $S(\boldsymbol{r})$ and $V(\boldsymbol{r})$ being the scalar and the vector potential, respectively, and where

$$S(\boldsymbol{r}) = \alpha_S \rho_S + \beta_S \rho_S^2 + \gamma_S \rho_S^3 + \delta_S \Delta \rho_S, \tag{3}$$

$$V(\boldsymbol{r}) = \alpha_V \rho_V + \gamma_V \rho_V^3 + \delta_V \Delta \rho_V + e\frac{1-\tau_3}{2} A^0 + \alpha_{TV} \tau_3 \rho_3 + \delta_{TV} \tau_3 \Delta \rho_3. \tag{4}$$

The pairing potential Δ reads as

$$\Delta(\boldsymbol{r}_1, \boldsymbol{r}_2) = V^{pp}(\boldsymbol{r}_1, \boldsymbol{r}_2) \kappa(\boldsymbol{r}_1, \boldsymbol{r}_2), \tag{5}$$

with the density-dependent zero-range pairing force V^{pp},

$$V^{pp}(\boldsymbol{r}_1, \boldsymbol{r}_2) = \frac{1}{2} V_0 (1 - P^\sigma) \delta(\boldsymbol{r}_1 - \boldsymbol{r}_2) \left(1 - \frac{\rho(\boldsymbol{r}_1)}{\rho_{\rm sat}}\right). \tag{6}$$

and the pairing tensor $\kappa = V^* U^T$.

2.2. The Lipkin–Nogami Method

The Lipkin–Nogami method [28–30] is an approximation to the variation after particle number projection. Its detailed formalism and its comparison with the exact projection method can be found in Ref. [26].

The application of the LN method to the framework of RHB gives a modification of the RHB equation, i.e., the RHB+LN equation [27]

$$\begin{pmatrix} h_D - \lambda - 2\lambda_2(1-2\rho) & \Delta \\ -\Delta^* & -h_D^* + \lambda + 2\lambda_2(1-2\rho^*) \end{pmatrix} \begin{pmatrix} U_k \\ V_k \end{pmatrix} = (E_k - \lambda_2) \begin{pmatrix} U_k \\ V_k \end{pmatrix}, \tag{7}$$

where λ_2 is given by

$$\lambda_2 = -\frac{1}{4} \frac{\mathrm{Tr}_2 \mathrm{Tr}_2 [(\kappa^* \rho) \bar{v} (\sigma \kappa)]}{[\mathrm{Tr}(\kappa \kappa^\dagger)]^2 - 2\mathrm{Tr}(\kappa \kappa^\dagger \kappa \kappa^\dagger)} \tag{8}$$

with ρ being the density matrix and $\sigma = 1 - \rho$ and $\bar{v}_{abcd} = \langle ab | V^{pp} | cd - dc \rangle$ being the antisymmetrized matrix elements of the pairing force V^{pp}. The trace Tr_2 means the summation only runs over the particle–particle channel [25].

After the approximate particle number projection, the total energy reads as [49]

$$E_{\mathrm{LN}} = \langle \hat{H} \rangle - \lambda_2 \langle (\Delta \hat{N})^2 \rangle. \tag{9}$$

Similarly, the physical observables should be calculated with the approximately particle number projected state. In particular, the LN occupation probabilities in canonical basis are given by [31,49]

$$w_k = v_k^2 + \overline{u^2 v^2} \frac{u_k^2 v_k^2 \overline{u^2 v^2 (u^2 - v^2)} - u_k^2 v_k^2 (u_k^2 - v_k^2) \overline{u^2 v^2}}{2(\overline{u^2 v^2})^3 + (\overline{u^2 v^2})^2 - 6\overline{u^2 v^2}\, \overline{u^4 v^4} - [\overline{u^2 v^2 (u^2 - v^2)}]^2} \tag{10}$$

with $\overline{x} = \sum_{k>0} x_k$.

3. Numerical Details

For the present investigation of Ca isotopes, the spherical RCHB calculations are adopted. It is noted that in Ref. [50], the DRHBc theory was used to calculate all the even–even nuclei with $8 \leq Z \leq 120$, and the authors found that the investigated Ca isotopes were all spherical. As mentioned above, instead of coordinate space [11], here the RCHB theory is solved in the DWS basis [42]. This is actually a simplification of the DRHBc theory with the assumption of spherical symmetry, i.e., the Hamiltonian matrix is expanded in j^π-blocks instead of m^π-blocks. Based on this, the LN correction is further implemented.

The relativistic density functional PC-PK1 [51] is employed in the particle–hole channel, and in the particle–particle channel, the density-dependent zero-range pairing force (6) is adopted, where the pairing strength $V_0 = -325$ MeV $\cdot$ fm^3 and the saturation density $\rho_{\mathrm{sat}} = 0.152$ fm^{-3} together with a pairing window of 100 MeV. The energy cutoff for the DWS basis in the Fermi sea is $E_{\mathrm{cut}}^+ = 300$ MeV. The angular momentum cutoff for the DWS basis is $J_{\mathrm{cut}} = 23/2\,\hbar$. The number of DWS basis states in the Dirac sea is taken to be the same as that in the Fermi sea. All these numerical details are well examined in the DRHBc mass table calculations [50,52–54], where the RHB equation is also solved in a spherical DWS basis.

In the RCHB+LN calculations, all the numerical details are taken to be the same as those in the RCHB calculations except the pairing strength, because the LN correction gives stronger pairing correlations with the same pairing force (cf. Figure 4a,b in Ref. [27]). Figure 1 shows the odd–even mass differences for Ca isotopes calculated by RCHB+LN in comparison with those in RCHB calculations, as well as the corresponding experimental data [55]. It is found that in RCHB+LN calculations, the odd–even mass differences of most Ca isotopes are overestimated when the pairing strength is chosen to be $V_0 = -325$ MeV $\cdot$ fm^3. Therefore, the pairing strength was readjusted to $V_0 = -300$ MeV $\cdot$ fm^3 in order to reproduce the experimental data.

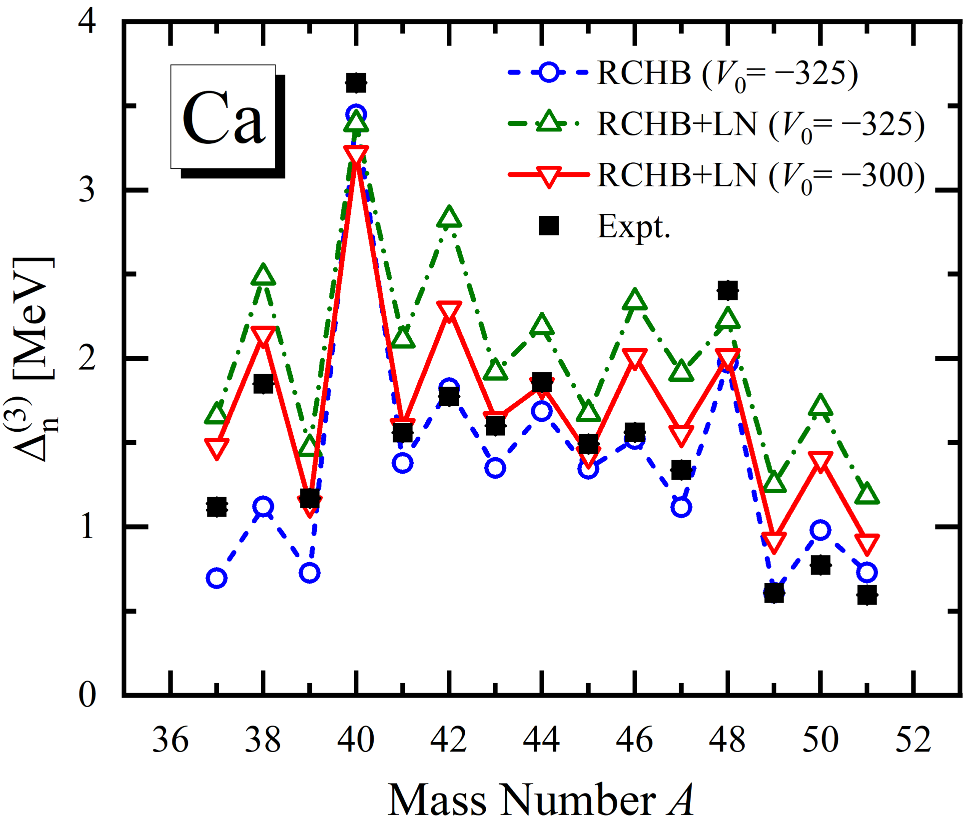

Figure 1. The odd–even differences of Ca isotopic chain in the relativistic continuum Hartree–Bogoliubov+Lipkin–Nogami (RCHB+LN) calculations versus the mass number for $V_0 = -325$ MeV · fm^3 (triangle) and for $V_0 = -300$MeV · fm^3 (inverted triangle). The experimental data [55] (square) and the results in RCHB calculations (circle) are shown for comparison.

4. Results and Discussion

The ground-state properties of even Ca isotopes calculated by RCHB and RCHB+LN are shown in Figure 2. The results of RCHB+LN with $V_0 = -325$ MeV · fm^3 are also shown for comparison. The binding energies per nucleon BE/A are shown in Figure 2a. It is found that larger BE/A are given by including the LN correction, while the trend does not change. The two-neutron separation energies S_{2n} are shown in Figure 2b. In RCHB results, kinks appear at the traditional magic or submagic numbers $N = 20$, 28, and 40. With LN correction, all the amplitudes of these kinks become smaller. At $N = 50$, however, there seems no kink for both the RCHB and RCHB+LN, indicating the disappearance of the traditional magic number $N = 50$ in Ca isotopes. In addition, in the region of $N > 40$, the nuclei become weakly-bound, and the S_{2n} decrease slowly both in the RCHB and RCHB+LN calculations. Such behavior of S_{2n} indicates the appearance of giant halos in the Ca isotopes. Moreover, both the RCHB and the RCHB+LN calculations show the two-neutron drip line of the Ca isotopic chain at $N = 60$. The root mean square (rms) neutron radii in even Ca isotopes are plotted in Figure 2c. The rms radii are nearly unchanged with the LN correction. In addition, from $N = 40$, the rms radii gradually deviate from the empirical $r_0 N^{1/3}$ formula as the neutron number increases. This behavior also indicates the possible existence of the halo or giant halo phenomena.

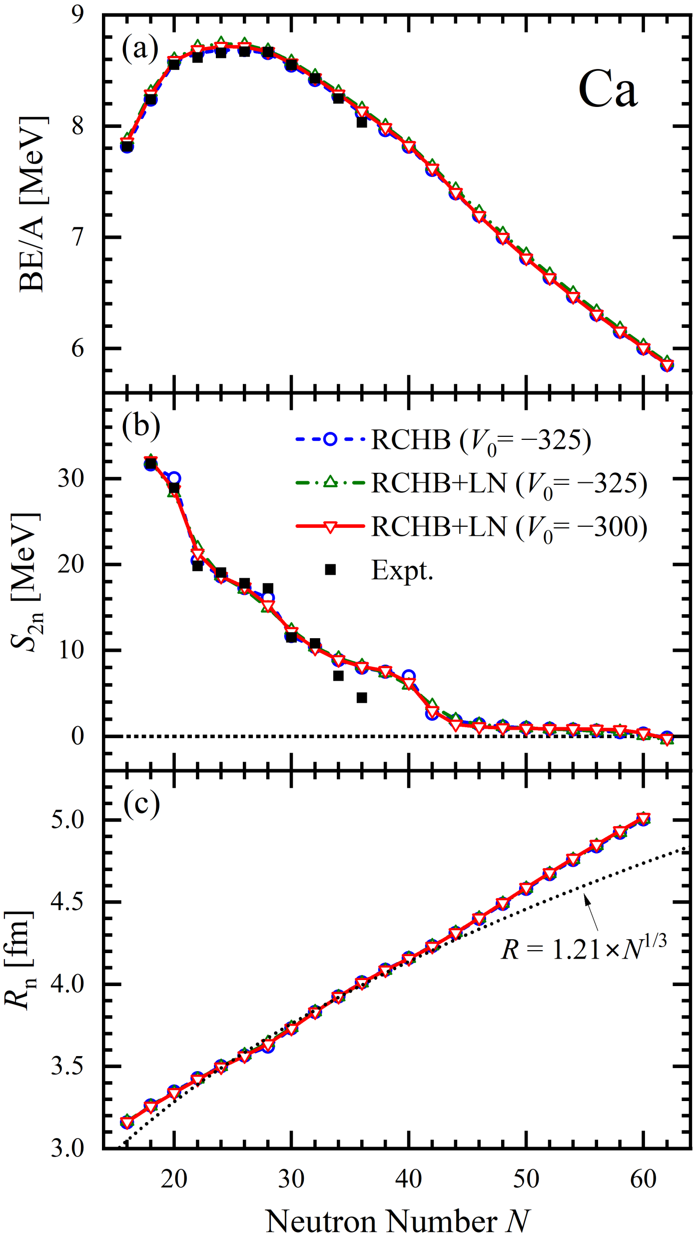

Figure 2. (color online) The ground-state properties of even Ca isotopes, including (**a**) the binding energies per nucleon BE/A, (**b**) the two-neutron separation energies S_{2n}, and (**c**) the root mean square neutron radii R_n obtained from the RCHB and RCHB+LN calculations. The experimental results (square) of BE/A and S_{2n}, as well as the empirical formula (dotted line) of R_n, are also shown for comparison.

Figure 3 shows the neutron density distributions of Ca isotopes derived from RCHB and RCHB+LN calculations. In the region of $N > 40$, the neutron density distribution of Ca isotopes with $A > 62$ are much more diffused than those of ^{60,62}Ca for both the RCHB and RCHB+LN. Combined with the S_{2n} and R_n results mentioned before, this indicates that $^{64-80}$Ca are halo nuclei but that ^{62}Ca is not, and the LN correction does not change the range of those with halo.

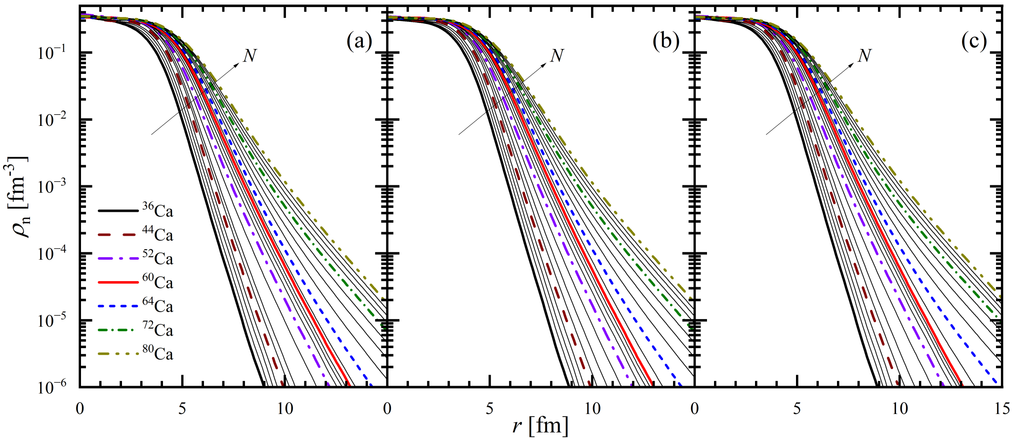

Figure 3. (color online) The neutron density distributions of even Ca isotopes obtained from RCHB+LN for (**b**) $V_0 = -325$ MeV $\cdot$ fm^3 and (**c**) $V_0 = -300$ MeV $\cdot$ fm^3 in comparison with (**a**) RCHB results for $V_0 = -325$ MeV $\cdot$ fm^3.

To see the impact of the LN correction more clearly, as in Refs. [13,14], we take ^{66}Ca as an example. Figure 4 shows its single-neutron levels in canonical basis around the Fermi surface, where the results of the RCHB with $V_0 = -325$ MeV $\cdot$ fm^3, RCHB+LN with $V_0 = -325$ MeV $\cdot$ fm^3, and RCHB+LN with $V_0 = -300$ MeV $\cdot$ fm^3 are plotted in the three panels, respectively. Comparison between these three calculations shows that the LN correction only slightly changes the energies and the occupation probabilities of the levels. For example, the energy and the occupation probability of the neutron $2d_{3/2}$ level with the largest difference are 2.05 MeV and 6.2% for the RCHB with $V_0 = -325$ MeV $\cdot$ fm^3, 1.96 MeV and 7.0% for the RCHB+LN with $V_0 = -325$ MeV $\cdot$ fm^3, and 1.87 MeV and 5.2% for the RCHB+LN with $V_0 = -300$ MeV $\cdot$ fm^3, respectively.

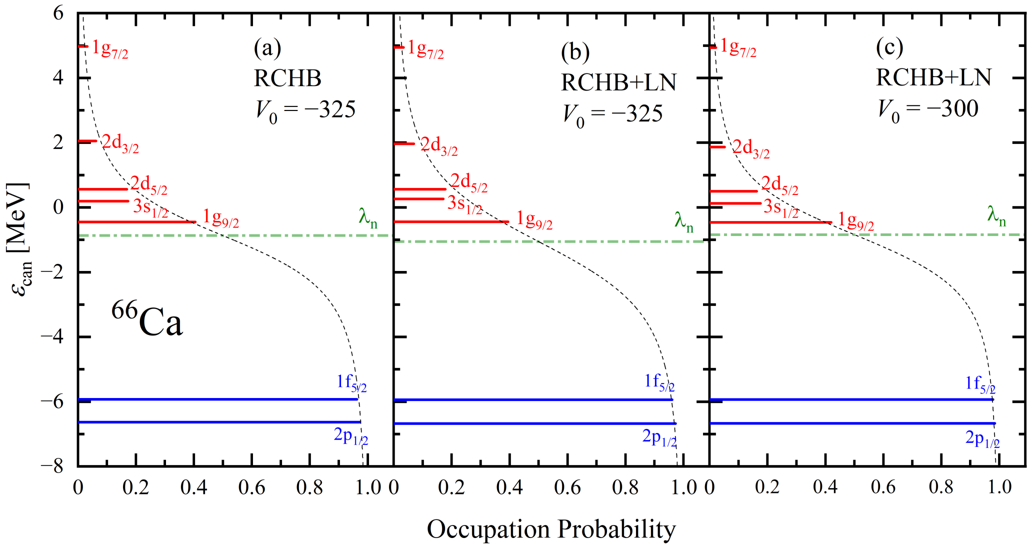

Figure 4. (color online) The single-neutron levels around the Fermi surface in the canonical basis for ^{66}Ca versus the occupation probability (v^2 for RCHB and w for RCHB+LN) obtained from RCHB+LN for (**b**) $V_0 = -325$ MeV $\cdot$ fm^3 and (**c**) $V_0 = -300$ MeV $\cdot$ fm^3 in comparison with (**a**) RCHB results for $V_0 = -325$ MeV $\cdot$ fm^3. The dash-dotted lines indicate the neutron Fermi surfaces. The dotted curves correspond to the BCS or BCS+LN formula with corresponding average pairing gap.

To further check the influence of the LN correction on the potential giant halo in ^{66}Ca, the rms radii of each single-neutron level around the Fermi surface in RCHB and RCHB+LN calculations are compared in Figure 5. The rms radius of the neutron $3s_{1/2}$ level is much larger than other neutron levels nearby both in RCHB and RCHB+LN. This shows that the neutron $3s_{1/2}$ level plays a crucial role in the giant halo in Ca isotopes, as was pointed out in Ref. [13]. With LN correction, when the same pairing strength $V_0 = -325\ \mathrm{MeV} \cdot \mathrm{fm}^3$ is employed, the rms radii of these single-neutron levels do not change much. Among them, the rms radius of the neutron $2d_{5/2}$ level changes most for about 0.04 fm. In contrast, when the pairing strength is readjusted to $V_0 = -300\ \mathrm{MeV} \cdot \mathrm{fm}^3$, although most of the radii do not change much, there are considerable changes in those of the neutron $3s_{1/2}$, $2d_{5/2}$, and $2d_{3/2}$ levels. Especially for neutron $3s_{1/2}$ level, its rms radius increases from 6.775 fm (RCHB, $V_0 = -325$) and 6.804 fm (RCHB+LN, $V_0 = -325$) to 7.100 fm (RCHB+LN, $V_0 = -300$).

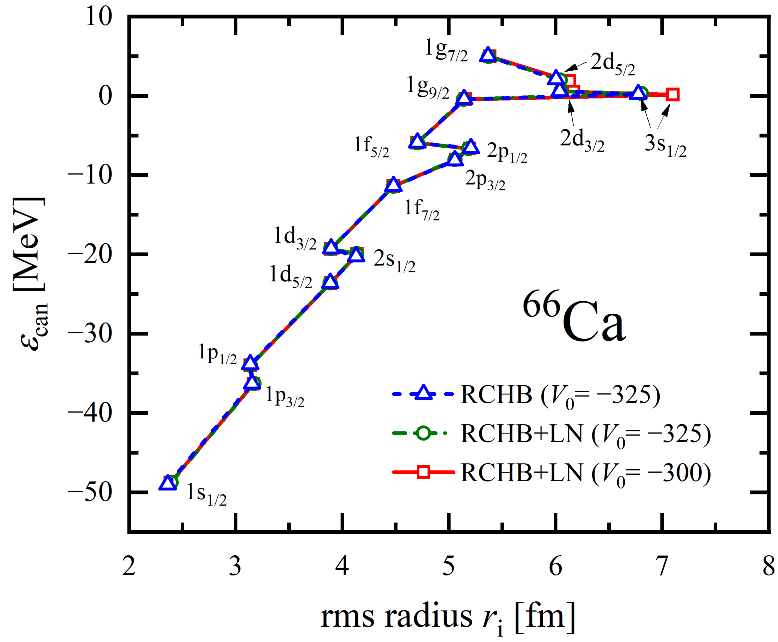

Figure 5. (color online) The single-particle energies in the canonical basis $\varepsilon_{\mathrm{can}}$ of each single-neutron level around the Fermi surface in ^{66}Ca versus its root mean square radius r_i.

As shown in Figure 4, there is a large shell gap between the $1g_{9/2}$ level and $1f_{5/2}$ level both in the RCHB and RCHB+LN, which corresponds to the submagic number $N = 40$. Thus, one can naturally take the levels below the $N = 40$ shell gap as the "core", and the remaining weakly bound levels and the levels in continuum above the shell gap as the "halo". Correspondingly, one can decompose the neutron density $\rho_n(\boldsymbol{r})$ into the "core" part and the "halo" part, as is plotted in Figure 6. The three panels show the results of the RCHB with $V_0 = -325\ \mathrm{MeV} \cdot \mathrm{fm}^3$, RCHB+LN with $V_0 = -325\ \mathrm{MeV} \cdot \mathrm{fm}^3$, and RCHB+LN with $V_0 = -300\ \mathrm{MeV} \cdot \mathrm{fm}^3$, respectively. The halo part surpasses the core part at about $r = 8$ fm and gradually domains with increasing r in all three calculations, indicating the halo structure in ^{66}Ca. The neutron numbers in the halo are 6.45 for both the RCHB and RCHB+LN with $V_0 = -325\ \mathrm{MeV} \cdot \mathrm{fm}^3$ and 6.25 for the RCHB+LN with $V_0 = -300\ \mathrm{MeV} \cdot \mathrm{fm}^3$. The results show that the LN correction does not change the appearance of giant halos in ^{66}Ca. On the one hand, under the same pairing strength, both the neutron number in the halo and the neutron density distribution of RCHB+LN are nearly unchanged in comparison with that of RCHB. On the other hand, with the pairing strength readjusted, the neutron density distribution of the RCHB+LN becomes slightly more diffused, although the neutron number in the halo becomes a little smaller.

To further analyze the neutron density, the density distributions of several single-neutron levels in the halo are also depicted in Figure 6. The neutron $3s_{1/2}$ level contributes to the halo most both in the RCHB and RCHB+LN. This can be seen more clearly in Figure 7, where the relative contributions to the total neutron density of these single-neutron levels are plotted. At $r = 15$ fm, the relative contribution of the neutron $3s_{1/2}$ level is about 50% in the RCHB with $V_0 = -325$ MeV $\cdot$ fm^3, about 48% in the RCHB+LN with $V_0 = -325$ MeV $\cdot$ fm^3, and about 55% in the RCHB+LN with $V_0 = -300$ MeV $\cdot$ fm^3. Such a result shows that with LN correction, when the pairing strength is $V_0 = -325$ MeV $\cdot$ fm^3, the neutron $3s_{1/2}$ level contributes slightly less to the giant halo in ^{66}Ca. In contrast, when the pairing strength is readjusted to $V_0 = -300$ MeV $\cdot$ fm^3, it contributes more. As the density distribution of neutron $3s_{1/2}$ level is more diffused than other levels nearby (cf. Figure 6), it is no wonder why the total neutron density becomes more diffused with LN correction and the readjusted pairing strength.

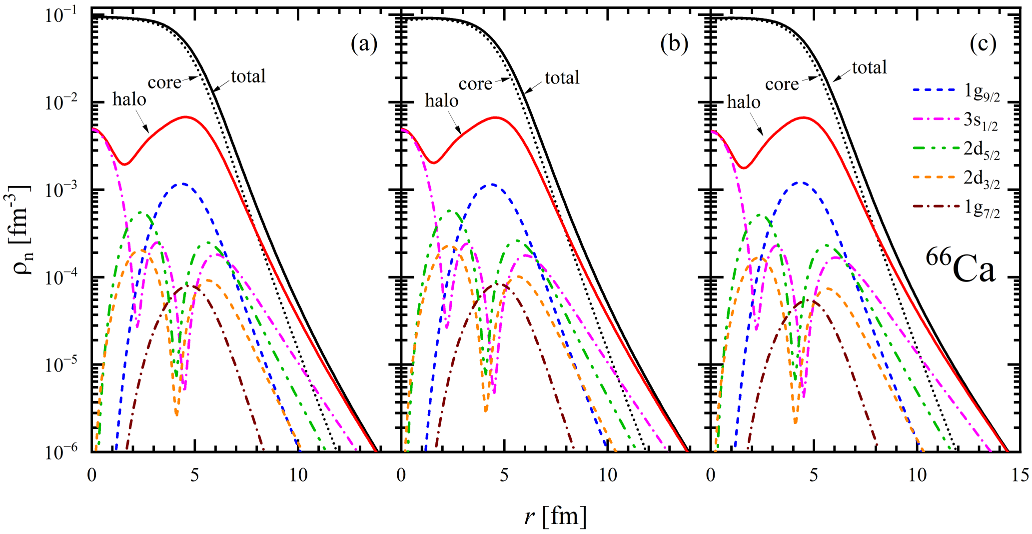

Figure 6. (color online) The total neutron density distribution of ^{66}Ca, as well as its decomposition into the core and the halo, obtained from RCHB+LN for (**b**) $V_0 = -325$ MeV $\cdot$ fm^3 and (**c**) $V_0 = -300$ MeV $\cdot$ fm^3 in comparison with (**a**) RCHB results for $V_0 = -325$ MeV $\cdot$ fm^3. Contributions from several single-neutron levels in the halo are also given.

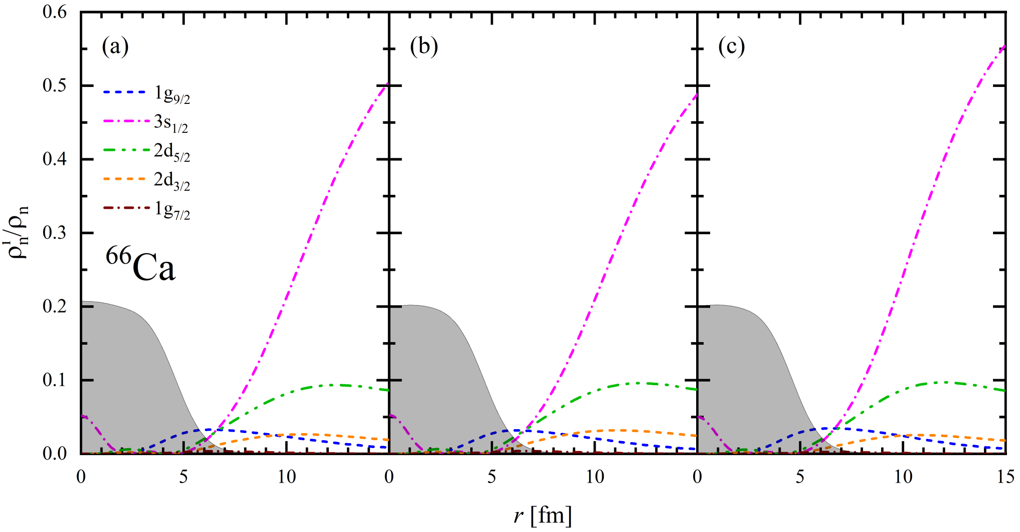

Figure 7. (color online) The relative contributions of several single-neutron levels in the halo of ^{66}Ca obtained from RCHB+LN for (**b**) $V_0 = -325$ MeV $\cdot$ fm^3 and (**c**) $V_0 = -300$ MeV $\cdot$ fm^3 in comparison with (**a**) RCHB results for $V_0 = -325$ MeV $\cdot$ fm^3. The shade areas indicate the total neutron density in arbitrary units.

5. Conclusions

In this paper, the impact of the Lipkin–Nogami (LN) method on giant halos has been investigated within the relativistic continuum Hartree–Bogoliubov (RCHB) theory. Here, the RHB and RHB+LN equations were solved in a spherical Dirac Woods–Saxon basis. Reproducing the odd–even mass differences of Ca isotopes, the pairing strength was readjusted to $V_0 = -300\ \mathrm{MeV} \cdot \mathrm{fm}^3$ for RCHB+LN. Comparing the ground-state properties of Ca isotopes calculated by the RCHB with $V_0 = -325\ \mathrm{MeV} \cdot \mathrm{fm}^3$, the RCHB+LN with $V_0 = -325\ \mathrm{MeV} \cdot \mathrm{fm}^3$, and the RCHB+LN with $V_0 = -300\ \mathrm{MeV} \cdot \mathrm{fm}^3$, this shows that the LN correction does not change the range of Ca isotopes with giant halos. Taking ^{66}Ca as an example, the neutron density distribution obtained with LN correction and readjusted pairing strength has been found to be slightly more diffused than that of the RCHB, which can be illustrated by the enlargement of the root mean square radius and the enhancement of the relative contribution for neutron $3s_{1/2}$ level.

Note that present results are limited to spherical halo nuclei, and the influence of the LN correction on the deformed halo nuclei is a topic to be investigated in the future. As the LN method is an approximation to the exact particle number projection method, how the exact particle number projection works on halo nuclei is an interesting topic. Besides halo phenomenon, neutron skin has also attracted much attention [56–58], and further investigation on it can be carried out. In addition, studies on odd nuclei are also important. For instance, in a recent work [48], the even–odd staggering of charge radii in Hg isotopes has been studied by the DRHBc theory and attributed to shape staggering. The even–odd staggering of charge radii in Ca isotopes is also interesting, which has attracted many theoretical efforts [59–63], and thus future work about it based on the DRHBc theory is welcome.

Author Contributions: Conceptualization, C.Z.; methodology, C.Z.; software, C.Z.; formal analysis, All authors; investigation, C.Z. and P.G.; writing—original draft preparation, C.Z.; writing—review and editing, All authors; visualization, C.Z.; project administration, X.J. All authors have read and agreed to the published version of the manuscript.

Funding: This work was partly supported by the National Natural Science Foundation of China under Grants No. 11935003, No. 12435006, No. 12141501, and No. 12475117; the State Key Laboratory of Nuclear Physics and Technology; Peking University under Grant No. NPT2023ZX03; and the National Key Laboratory of Neutron Science and Technology under Grant No. NST202401016.

Data Availability Statement: The dataset can be accessed upon request to the corresponding author.

Acknowledgments: The authors are indebted to J. Meng and S.-Q. Zhang for their constructive guidance and valuable suggestions. This work was supported by High-performance Computing Platform of Peking University. Helpful discussions with K.-Y. Zhang, C. Pan, and the members of the DRHBc Mass Table Collaboration are highly appreciated.

Conflicts of Interest: The authors declare no conflicts of interest.

References

1. Vretenar, D.; Afanasjev, A.; Lalazissis, G.; Ring, P. Relativistic Hartree-Bogoliubov theory: Static and dynamic aspects of exotic nuclear structure. *Phys. Rep.* **2005**, *409*, 101–259. [CrossRef]
2. Gade, A.; Glasmacher, T. In-beam nuclear spectroscopy of bound states with fast exotic ion beams. *Prog. Part. Nucl. Phys.* **2008**, *60*, 161–224. [CrossRef]
3. Otsuka, T.; Gade, A.; Sorlin, O.; Suzuki, T.; Utsuno, Y. Evolution of shell structure in exotic nuclei. *Rev. Mod. Phys.* **2020**, *92*, 015002. [CrossRef]
4. Yamaguchi, T.; Koura, H.; Litvinov, Y.; Wang, M. Masses of exotic nuclei. *Prog. Part. Nucl. Phys.* **2021**, *120*, 103882. [CrossRef]
5. Tanihata, I.; Hamagaki, H.; Hashimoto, O.; Shida, Y.; Yoshikawa, N.; Sugimoto, K.; Yamakawa, O.; Kobayashi, T.; Takahashi, N. Measurements of Interaction Cross Sections and Nuclear Radii in the Light *p*-Shell Region. *Phys. Rev. Lett.* **1985**, *55*, 2676–2679. [CrossRef]
6. Zhang, K.Y.; Papakonstantinou, P.; Mun, M.H.; Kim, Y.; Yan, H.; Sun, X.X. Collapse of the $N = 28$ shell closure in the newly discovered ^{39}Na nucleus and the development of deformed halos towards the neutron dripline. *Phys. Rev. C* **2023**, *107*, l041303. [CrossRef]

7. Kobayashi, T.; Yamakawa, O.; Omata, K.; Sugimoto, K.; Shimoda, T.; Takahashi, N.; Tanihata, I. Projectile Fragmentation of the Extremely Neutron-Rich Nucleus ^{11}Li at 0.79 GeV/nucleon. *Phys. Rev. Lett.* **1988**, *60*, 2599–2602. [CrossRef] [PubMed]
8. Orr, N.A.; Anantaraman, N.; Austin, S.M.; Bertulani, C.A.; Hanold, K.; Kelley, J.H.; Morrissey, D.J.; Sherrill, B.M.; Souliotis, G.A.; Thoennessen, M.; et al. Momentum distributions of ^{9}Li fragments following the breakup of ^{11}Li. *Phys. Rev. Lett.* **1992**, *69*, 2050–2053. [CrossRef]
9. Ieki, K.; Sackett, D.; Galonsky, A.; Bertulani, C.A.; Kruse, J.J.; Lynch, W.G.; Morrissey, D.J.; Orr, N.A.; Schulz, H.; Sherrill, B.M.; et al. Coulomb dissociation of ^{11}Li. *Phys. Rev. Lett.* **1993**, *70*, 730–733. [CrossRef]
10. Meng, J.; Ring, P. Relativistic Hartree-Bogoliubov Description of the Neutron Halo in ^{11}Li. *Phys. Rev. Lett.* **1996**, *77*, 3963–3966. [CrossRef] [PubMed]
11. Meng, J. Relativistic continuum Hartree-Bogoliubov theory with both zero range and finite range Gogny force and their application. *Nucl. Phys. A* **1998**, *635*, 3–42. [CrossRef]
12. Meng, J.; Ring, P. Giant Halo at the Neutron Drip Line. *Phys. Rev. Lett.* **1998**, *80*, 460–463. [CrossRef]
13. Meng, J.; Toki, H.; Zeng, J.Y.; Zhang, S.Q.; Zhou, S.G. Giant halo at the neutron drip line in Ca isotopes in relativistic continuum Hartree-Bogoliubov theory. *Phys. Rev. C* **2002**, *65*, 041302. [CrossRef]
14. Terasaki, J.; Zhang, S.Q.; Zhou, S.G.; Meng, J. Giant halos in relativistic and nonrelativistic approaches. *Phys. Rev. C* **2006**, *74*, 054318. [CrossRef]
15. Sandulescu, N.; Geng, L.S.; Toki, H.; Hillhouse, G.C. Pairing correlations and resonant states in the relativistic mean field theory. *Phys. Rev. C* **2003**, *68*, 054323. [CrossRef]
16. Zhang, S.S.; Xu, X.D.; Peng, J.P. Hints of giant halo in Zr isotopes by resonant RMF+ACCC+BCS approach. *Eur. Phys. J. A* **2012**, *48*. [CrossRef]
17. Ding, K.M.; Shi, M.; Guo, J.Y.; Niu, Z.M.; Liang, H. Resonant-continuum relativistic mean-field plus BCS in complex momentum representation. *Phys. Rev. C* **2018**, *98*, 014316. [CrossRef]
18. Cao, X.N.; Ding, K.M.; Shi, M.; Liu, Q.; Guo, J.Y. Exploration of the exotic structure in Ce isotopes by the relativistic point-coupling model combined with complex momentum representation. *Phys. Rev. C* **2020**, *102*, 044313. [CrossRef]
19. Long, W.H.; Ring, P.; Meng, J.; Van Giai, N.; Bertulani, C.A. Nuclear halo structure and pseudospin symmetry. *Phys. Rev. C* **2010**, *81*, 031302. [CrossRef]
20. Grasso, M.; Yoshida, S.; Sandulescu, N.; Van Giai, N. Giant neutron halos in the non-relativistic mean field approach. *Phys. Rev. C* **2006**, *74*, 064317. [CrossRef]
21. Zhang, Y.; Matsuo, M.; Meng, J. Pair correlation of giant halo nuclei in continuum Skyrme-Hartree-Fock-Bogoliubov theory. *Phys. Rev. C* **2012**, *86*, 054318. [CrossRef]
22. Qu, X.Y.; Zhang, Y. Canonical states in continuum Skyrme Hartree-Fock-Bogoliubov theory with Green's function method. *Phys. Rev. C* **2019**, *99*, 014314. [CrossRef]
23. Sun, T.T. Green's function method in covariant density functional theory. *Sci. Sin.-Phys. Mech. Astron.* **2015**, *46*, 012006. (In Chinese) [CrossRef]
24. Qu, X.Y.; Tong, H.; Zhang, S.Q. Canonical states in relativistic continuum theory with the Green's function method: Neutrons in continuum of zirconium giant-halo nuclei. *Phys. Rev. C* **2022**, *105*, 014326. [CrossRef]
25. Ring, P.; Schuck, P. *The Nuclear Many-Body Problem*; Springer: Berlin, Germany, 2004.
26. Sheikh, J.A.; Dobaczewski, J.; Ring, P.; Robledo, L.M.; Yannouleas, C. Symmetry restoration in mean-field approaches. *J. Phys. G Nucl. Part. Phys.* **2021**, *48*, 123001. [CrossRef]
27. Afanasjev, A.; Ring, P.; König, J. Cranked relativistic Hartree–Bogoliubov theory: Formalism and application to the superdeformed bands in the A∼190 region. *Nucl. Phys. A* **2000**, *676*, 196–244. [CrossRef]
28. Lipkin, H.J. Collective motion in many-particle systems. *Ann. Phys.* **1960**, *9*, 272–291. [CrossRef]
29. Nogami, Y. Improved Superconductivity Approximation for the Pairing Interaction in Nuclei. *Phys. Rev.* **1964**, *134*, B313–B321. [CrossRef]
30. Pradhan, H.; Nogami, Y.; Law, J. Study of approximations in the nuclear pairing-force problem. *Nucl. Phys. A* **1973**, *201*, 357–368. [CrossRef]
31. Bennour, L.; Heenen, P.H.; Bonche, P.; Dobaczewski, J.; Flocard, H. Charge distributions of ^{208}Pb, ^{206}Pb, and ^{205}Tl and the mean-field approximation. *Phys. Rev. C* **1989**, *40*, 2834–2839. [CrossRef]
32. Shi, H.; Wang, X.B.; Dong, G.X.; Wang, H. Abnormal odd-even staggering behavior around ^{132}Sn studied by density functional theory. *Chin. Phys. C* **2020**, *44*, 094108. [CrossRef]
33. Raj, R.; Rustgi, M.L. Modified Tamm-Dancoff approximation calculations using Lipkin-Nogami approach. *Phys. Rev. C* **1982**, *26*, 243–248. [CrossRef]
34. Raj, R.; Rustgi, M.L. Odd Ni isotopes in the Lipkin-Nogami approach. *Phys. Rev. C* **1983**, *28*, 935–937. [CrossRef]
35. Terasaki, J.; Heenen, P.H.; Bonche, P.; Dobaczewski, J.; Flocard, H. Superdeformed rotational bands with density dependent pairing interactions. *Nucl. Phys. A* **1995**, *593*, 1–20. [CrossRef]
36. Afanasjev, A.V.; König, J.; Ring, P. Cranked relativistic Hartree-Bogoliubov theory: Superdeformed bands in the $A \sim 190$ region. *Phys. Rev. C* **1999**, *60*, 051303. [CrossRef]
37. Hung, N.Q.; Dang, N.D. Canonical and microcanonical ensemble descriptions of thermal pairing within BCS and quasiparticle random-phase approximation. *Phys. Rev. C* **2010**, *81*, 057302. [CrossRef]

38. Saleh Yousef, M.; Elsharkawy, H.; Rashed, N. Matrix elements of the two-neutrino double beta decay of ^{76}Ge using deformed BCS and Lipkin–Nogami approaches. *Nucl. Phys. A* **2018**, *975*, 97–106. [CrossRef]
39. Meng, J.; Toki, H.; Zhou, S.; Zhang, S.; Long, W.; Geng, L. Relativistic continuum Hartree Bogoliubov theory for ground-state properties of exotic nuclei. *Prog. Part. Nucl. Phys.* **2006**, *57*, 470–563. [CrossRef]
40. Meng, J.; Zhou, S.G. Halos in medium-heavy and heavy nuclei with covariant density functional theory in continuum. *J. Phys. G: Nucl. Part. Phys.* **2015**, *42*, 093101. [CrossRef]
41. Kucharek, H.; Ring, P. Relativistic field theory of superfluidity in nuclei. *Z. Phys. A* **1991**, *339*, 23–35. [CrossRef]
42. Zhou, S.G.; Meng, J.; Ring, P. Spherical relativistic Hartree theory in a Woods-Saxon basis. *Phys. Rev. C* **2003**, *68*, 034323. [CrossRef]
43. Zhou, S.G.; Meng, J.; Ring, P.; Zhao, E.G. Neutron halo in deformed nuclei. *Phys. Rev. C* **2010**, *82*, 011301. [CrossRef]
44. Sun, X.X.; Zhao, J.; Zhou, S.G. Shrunk halo and quenched shell gap at $N = 16$ in ^{22}C: Inversion of *sd* states and deformation effects. *Phys. Lett. B* **2018**, *785*, 530–535. [CrossRef]
45. Zhang, K.; He, X.; Meng, J.; Pan, C.; Shen, C.; Wang, C.; Zhang, S. Predictive power for superheavy nuclear mass and possible stability beyond the neutron drip line in deformed relativistic Hartree-Bogoliubov theory in continuum. *Phys. Rev. C* **2021**, *104*, l021301. [CrossRef]
46. Choi, Y.B.; Lee, C.H.; Mun, M.H.; Kim, Y. Bubble nuclei with shape coexistence in even-even isotopes of Hf to Hg. *Phys. Rev. C* **2022**, *105*, 024306. [CrossRef]
47. Guo, P.; Pan, C.; Zhao, Y.C.; Du, X.K.; Zhang, S.Q. Prolate-shape dominance in atomic nuclei within the deformed relativistic Hartree-Bogoliubov theory in continuum. *Phys. Rev. C* **2023**, *108*, 014319. [CrossRef]
48. Mun, M.H.; Kim, S.; Cheoun, M.K.; So, W.; Choi, S.; Ha, E. Odd-even shape staggering and kink structure of charge radii of Hg isotopes by the deformed relativistic Hartree–Bogoliubov theory in continuum. *Phys. Lett. B* **2023**, *847*, 138298. [CrossRef]
49. Nikšić, T.; Vretenar, D.; Ring, P. Beyond the relativistic mean-field approximation. II. Configuration mixing of mean-field wave functions projected on angular momentum and particle number. *Phys. Rev. C* **2006**, *74*, 064309. [CrossRef]
50. Zhang, K.; Cheoun, M.K.; Choi, Y.B.; Chong, P.S.; Dong, J.; Dong, Z.; Du, X.; Geng, L.; Ha, E.; He, X.T.; et al. Nuclear mass table in deformed relativistic Hartree–Bogoliubov theory in continuum, I: Even–even nuclei. *At. Data Nucl. Data Tables* **2022**, *144*, 101488. [CrossRef]
51. Zhao, P.W.; Li, Z.P.; Yao, J.M.; Meng, J. New parametrization for the nuclear covariant energy density functional with a point-coupling interaction. *Phys. Rev. C* **2010**, *82*, 054319. [CrossRef]
52. Zhang, K.; Cheoun, M.K.; Choi, Y.B.; Chong, P.S.; Dong, J.; Geng, L.; Ha, E.; He, X.; Heo, C.; Ho, M.C.; et al. Deformed relativistic Hartree-Bogoliubov theory in continuum with a point-coupling functional: Examples of even-even Nd isotopes. *Phys. Rev. C* **2020**, *102*, 024314. [CrossRef]
53. Pan, C.; Cheoun, M.K.; Choi, Y.B.; Dong, J.; Du, X.; Fan, X.H.; Gao, W.; Geng, L.; Ha, E.; He, X.T.; et al. Deformed relativistic Hartree-Bogoliubov theory in continuum with a point-coupling functional. II. Examples of odd Nd isotopes. *Phys. Rev. C* **2022**, *106*, 014316. [CrossRef]
54. Guo, P.; Cao, X.; Chen, K.; Chen, Z.; Cheoun, M.K.; Choi, Y.B.; Lam, P.C.; Deng, W.; Dong, J.; Du, P.; et al. Nuclear mass table in deformed relativistic Hartree–Bogoliubov theory in continuum, II: Even-Z nuclei. *At. Data Nucl. Data Tables* **2024**, *158*, 101661. [CrossRef]
55. Wang, M.; Huang, W.; Kondev, F.; Audi, G.; Naimi, S. The AME 2020 atomic mass evaluation (II). Tables, graphs and references. *Chin. Phys. C* **2021**, *45*, 030003. [CrossRef]
56. Centelles, M.; Roca-Maza, X.; Viñas, X.; Warda, M. Origin of the neutron skin thickness of ^{208}Pb in nuclear mean-field models. *Phys. Rev. C* **2010**, *82*, 054314. [CrossRef]
57. Roca-Maza, X.; Centelles, M.; Viñas, X.; Warda, M. Neutron Skin of ^{208}Pb, Nuclear Symmetry Energy, and the Parity Radius Experiment. *Phys. Rev. Lett.* **2011**, *106*, 252501. [CrossRef] [PubMed]
58. Warda, M.; Centelles, M.; Viñas, X.; Roca-Maza, X. Influence of the single-particle structure on the nuclear surface and the neutron skin. *Phys. Rev. C* **2014**, *89*, 064302. [CrossRef]
59. Fayans, S.; Tolokonnikov, S.; Trykov, E.; Zawischa, D. Nuclear isotope shifts within the local energy-density functional approach. *Nucl. Phys. A* **2000**, *676*, 49–119. [CrossRef]
60. Reinhard, P.G.; Nazarewicz, W. Toward a global description of nuclear charge radii: Exploring the Fayans energy density functional. *Phys. Rev. C* **2017**, *95*, 064328. [CrossRef]
61. Miller, A.J.; Minamisono, K.; Klose, A.; Garand, D.; Kujawa, C.; Lantis, J.D.; Liu, Y.; Maaß, B.; Mantica, P.F.; Nazarewicz, W.; et al. Proton superfluidity and charge radii in proton-rich calcium isotopes. *Nat. Phys.* **2019**, *15*, 432–436. [CrossRef]
62. An, R.; Geng, L.S.; Zhang, S.S. Novel ansatz for charge radii in density functional theories. *Phys. Rev. C* **2020**, *102*, 024307. [CrossRef]
63. Yang, D.; Rong, Y.T.; An, R.; Shi, R.X. Potential signature of new magicity from universal aspects of nuclear charge radii. *arXiv* **2024**, arXiv:2411.03076. [CrossRef]